Conformational Equilibria in Polypeptides.
II. Dihedral-Angle Distribution in Antamanide Based on Three-Bond Coupling Information

Jürgen M. Schmidt

*Institut für Biophysikalische Chemie, Johann Wolfgang Goethe-Universität, Biozentrum N230,
Marie-Curie-Strasse 9, D-60439 Frankfurt am Main, Germany*

IN MEMORY OF PROFESSOR THEODOR WIELAND

The use of ^3J coupling information in deriving dihedral-angle restraints for polypeptide-structure determination in the presence of conformational equilibria is illustrated with *antamanide,* cyclo-(–Val^1–Pro^2–Pro^3–Ala^4–Phe^5–Phe^6–Pro^7–Pro^8–Phe^9–Phe^{10}–). The experimental basis comprises accurate three-bond coupling constants as obtained from both homonuclear [C. Griesinger, O. W. Sørensen, and R. R. Ernst, *J. Magn. Reson.* **75,** 474 (1987)] and heteronuclear [J. M. Schmidt, *J. Magn. Reson.* **124,** 298 (1997)] exclusive correlation spectroscopy (E.COSY). For the backbone and side-chain dihedral angles in the nonproline residues, ϕ and χ_1, respectively, probability-distribution functions are derived and evaluated on the basis of χ^2 statistics and significance estimates. Various motional models are considered in the quantitative compilation of molecular-geometry parameters from spin-system parameters. From the ^3J coupling analysis, antamanide is found to possess a very flexible structure which is consistent with the results previously obtained in homonuclear NOE and $^{13}C-T_1$ relaxation studies. To fully agree with experiment, rotamer equilibria must be assumed for almost all of the torsions investigated in the peptide. © 1997 Academic Press

INTRODUCTION

Dihedral-angle constraints as derived from ^3J coupling information play an increasing role in the process of determining the three-dimensional structure of polypeptides by NMR spectroscopy (*1–6*). With modern experimental multidimensional NMR techniques using isotope-enriched biomolecules along with proton-signal detection, almost any desired three-bond J coupling constant can be measured (*7–9*). Meanwhile, the amount of coupling data collected that potentially contributes to the experimental basis for molecular modeling follows closely the amount of distance information obtained from the measurement of NOE cross-relaxation rates. However, while the dependence of the NOE effect on the internuclear distance is known in detail (*10–12*), the quantitative interpretation of coupling constants in terms of conformational restrictions is not as well developed.

The backbone of a polypeptide fragment contains three main-chain torsion angles defined by the IUPAC/IUB conventions (*13*) to relate to various pairs of coupled nuclei. The dihedral angle ϕ (C$'_{i-1}$–N$'_i$–C$^\alpha_i$–C$'_i$) of residue i provides four $^3J_{HH}$ or $^3J_{HC}$ coupling constants to be measured by either homo- or heteronuclear correlation experiments. In contrast, only a single useful $^3J_{HN}$ coupling determines the dihedral angle ψ (N$'_i$–C$^\alpha_i$–C$'_i$–N$'_{i+1}$). The conformation of the dihedral angle ω (C$^\alpha_i$–C$'_i$–N$'_{i+1}$–C$^\alpha_{i+1}$), which may be determined by a single $^3J_{HC}$ heteronuclear coupling, is only of qualitative concern as the peptide bond usually adopts an almost planar orientation, either *cis* or *trans* configured. Of the numerous side-chain dihedral angles encountered in the various amino acids, the dihedral angle χ_1 (N$'_i$–C$^\alpha_i$–C$^\beta_i$–C$^\gamma_i$) has the largest impact on the spatial orientation of the side-chain atoms.

According to Karplus (*14, 15*), the dependence of the three-bond J coupling constant on the dihedral angle θ, which is subtended by the three successive covalent bonds that connect the coupled nuclei, is embodied in the relation

$$^3J(\theta) = A \cos^2(\theta) + B \cos(\theta) + C, \qquad [1]$$

where A, B, and C are empirical coefficients given in hertz. Theoretical as well as experimental studies have provided proper parametrizations for the different types of dihedral angles relevant to amino-acid conformation (*16*). An additive increment $\Delta\theta$ establishes the correct phase relation between the dihedral angle θ and one of the heavy-atom torsions, ϕ, ψ, ω, χ_1, etc. Table 1 summarizes Karplus coefficients and dihedral-angle phase increments relevant to torsion-angle analysis in polypeptides.

The intrinsic degeneracy of the Karplus relation in Eq. [1] implies a general nonuniqueness in the solution for the dihedral-angle argument from a single vicinal J coupling constant (Fig. 1). To resolve the ambiguity between the four values usually obtained, an equivalent number of independent units of information, i.e., four experimental data, may

<div align="center">

TABLE 1

Karplus Coefficients (Hz) for the Three-Bond Connectivities Encountered in Amino-Acid Backbone and Side-Chain Torsions

</div>

| θ	$\Delta\theta$ (°)	Coupling	$\Delta\theta$ (°)	Alternate coupling		Karplus coefficients[a]			Ref.[b]	Source and comments
						A	B	C		
ϕ	−60	$^3J(\text{H}^\text{N}, \text{H}^{\alpha(2)})$	+60	$^3J(\text{H}^\text{N}, \text{H}^{\alpha 3})$	*	9.4	−1.1	0.4	(1)	From various amino-acid derivatives
						5.4	−1.3	2.2	(2)	Ferrichrome curve
						6.4	−1.4	1.9	(3)	BPTI curve
						6.7	−1.3	1.5	(4)	Barnase curve
						6.51	−1.76	1.60	(5)	SNase curve
						6.40	−1.54	1.65	(6)	Ab initio RHF/6-31G* calculations
	±180	$^3J(\text{H}^\text{N}, \text{C}'_i)$			*	5.7	−2.7	0.1	(7)	Ab initio calculations
						4.0	−1.1	0.1	(8)[c]	From ubiquitin
	+60	$^3J(\text{H}^\text{N}, \text{C}^\beta)$			*	4.7	−1.5	−0.2	(7)	Ab initio calculations
	+120	$^3J(\text{H}^\alpha, \text{C}'_{i-1})$				4.5	−1.3	−1.2	(7)	Ab initio calculations
					*	9.0	−4.4	−0.8	(9)	From various amino-acid derivatives
ψ	−120	$^3J(\text{H}^\alpha, \text{N}'_{i+1})$				−4.6	3.0	0.8	(9)	From various peptides
						−5.25	2.23	0.93	(10)	Ab initio INDO/SCF-MO calculations
						−0.88	0.61	−0.27	(8)[c]	From ubiquitin
ω	±180	$^3J(\text{C}^\alpha, \text{H}^\text{N}_{i+1})$							(11)	cis 0.0 Hz ($\omega = 180°$), trans 7.1 Hz ($\omega = 0°$)
χ_1	−120	$^3J(\text{H}^{\alpha,} \text{H}^{\beta 2})$	±0	$^3J(\text{H}^{\alpha,} \text{H}^{\beta(3)})$		10.2	−1.8	1.9	(1)	From various amino-acid derivatives
						9.4	−1.4	1.6	(12)	From various amino-acid derivatives
					*	9.5	−1.6	1.8	(13)	From ornithyl residues in ferrichromes
	+120	$^3J(\text{H}^\alpha, \text{C}^{\gamma(1)})$	−120	$^3J(\text{H}^\alpha, \text{C}^{\gamma 2})$		10.2	−1.3	0.2	(14)	From ornithyl $^3J(\text{C}^\alpha, \text{H}^\gamma)$ in alumichrome
					*	7.1	−1.0	0.7	(15)	INDO calculations on propane
	+120	$^3J(\text{N}', \text{H}^{\beta 2})$	−120	$^3J(\text{N}', \text{H}^{\beta 3})$		−4.4	1.2	0.1	(16)	From alumichrome
					*	−3.75	0.26	−0.54	(17)	From ABCO compound
	±0	$^3J(\text{C}', \text{H}^{\beta 2})$	+120	$^3J(\text{C}', \text{H}^{\beta 3})$	*	7.20	−2.04	0.60	(17)	From ABCO compound
									(1)	gauche 0.4–1.5 Hz, trans 7.6–11.9 Hz

[a] Coefficients to be used with equation $^3J(\theta) = A\cos^2\theta + B\cos\theta + C$. Asterisks mark the parametrizations used for preparing Fig. 1 and for the dihedral-angle analysis in antamanide.

[b] (1) V. F. Bystrov, *Prog. NMR Spectrosc.* **10,** 41 (1976); V. F. Bystrov, V. T. Ivanov, S. L. Portnova, T. A. Balashova, and Y. A. Ouchinnikov, *Tetrahedron* **29,** 873 (1973). (2) A. DeMarco, M. Llinás, and K. Wüthrich, *Biopolymers* **17,** 636 (1978). (3) A. Pardi, M. Billeter, and K. Wüthrich, *J. Mol. Biol.* **180,** 741 (1984). (4) S. Ludvigsen, K. V. Andersen, and F. M. Poulsen, *J. Mol. Biol.* **217,** 731 (1991). (5) G. W. Vuister and A. Bax, *J. Am. Chem. Soc.* **115,** 7772 (1993). (6) A. S. Edison, J. L. Markley, and F. Weinhold, *J. Biomol. NMR* **4,** 519 (1994). (7) V. N. Solkan and V. F. Bystrov, *Bull Acad. Sci. USSR (Div. Chem. Sci.)* **23,** 1232 (1974). (8) A. C. Wang and A. Bax, *J. Am. Chem. Soc.* **117,** 1810 (1995). (9) V. F. Bystrov, Yu. D. Gavrilov, and V. N. Solkan, *J. Magn. Reson.* **19,** 123 (1975). (10) M. Barfield and H. L. Gearhart, *Mol. Phys.* **27,** 899 (1974). (11) D. E. Dorman and F. A. Bovey, *J. Org. Chem* **38,** 1719 (1973). (12) K. D. Kopple, G. R. Wiley, and R. Tauke, *Biopolymers* **12,** 627 (1973). (13) A. DeMarco, M. Llinás, and K. Wüthrich, *Biopolymers* **17,** 617 (1978). (14) A. DeMarco and M. Llinás, *Biochemistry* **18,** 3846 (1979). (15) R. Wasylishen and T. Schaefer, *Can. J. Chem.* **50,** 2710 (1972). (16) A. DeMarco, M. Llinás, and K. Wüthrich, *Biopolymers* **17,** 2727 (1978). (17) A. J. Fischman, D. H. Live, H. R. Wyssbrod, W. C. Agosta, and D. Cowburn, *J. Am. Chem. Soc.* **102,** 2533 (1980).

[c] Unfortunately, Wang and Bax incorporate into the coefficient B of Eq. [1] the effect of α 180° phase shift by defining the dihedral angle ϕ ($\text{H}^\text{N}_i-\text{N}'_i-\text{C}^\alpha_i-\text{C}'_i$) instead of the usual IUPAC/IUB convention ϕ ($\text{C}'_{i-1}-\text{N}'_i-\text{C}^\alpha_i-\text{C}'_i$), likewise for ψ ($\text{H}^\alpha_i-\text{C}^\alpha_i-\text{C}'_i-\text{N}'_{i+1}$) instead of ψ ($\text{N}'_i-\text{C}^\alpha_i-\text{C}'_i-\text{N}'_{i+1}$). To alleviate the comparison, their B values are negated here requiring the phase increments be taken into account as indicated.

be required. Since the Karplus relation of Eq. [1] is expressed in terms of only three coefficients, a mirror-image symmetry of the dihedral-angle dependence with respect to the origin $\theta = 0°$ is introduced. Such a constraint removes one degree of freedom, and three coupling constants are in essence sufficient for dihedral-angle determination. This conclusion is based on the critical assumptions that (i) the three coupling constants measured are associated with relative phase increments $\Delta\Delta\theta$ of 120° according to Table 1, and (ii) that the empirical Karplus coefficients used are strictly valid. It has been stated previously (17) that the study of two coupling constants that depend differently on the same torsional angle

already provides more conformational information than does a study of either coupling constant alone, given that their associated phase increments $\Delta\theta$ differ significantly from 0° and 180°. Situations in which the relative phase is 180°, e.g., for the pair of coupling constants associated with the amino-acid backbone torsion ϕ, $^3J(\text{H}^\text{N}, \text{H}^\alpha)$ and $^3J(\text{H}^\alpha, \text{C}'_{i-1})$, might nevertheless contribute more than a single piece of information because the absolute maxima of the Karplus curves are at reversed positions (18). A pair of two coupling constants with $\Delta\Delta\theta = 0°$, e.g., $^3J(\text{H}^\alpha, \text{C}^\gamma)$ and $^3J(\text{C}', \text{H}^{\beta 3})$ relevant to the amino-acid side-chain torsion χ_1, cannot fix two degrees of freedom because the dihedral-angle dependences bear re-
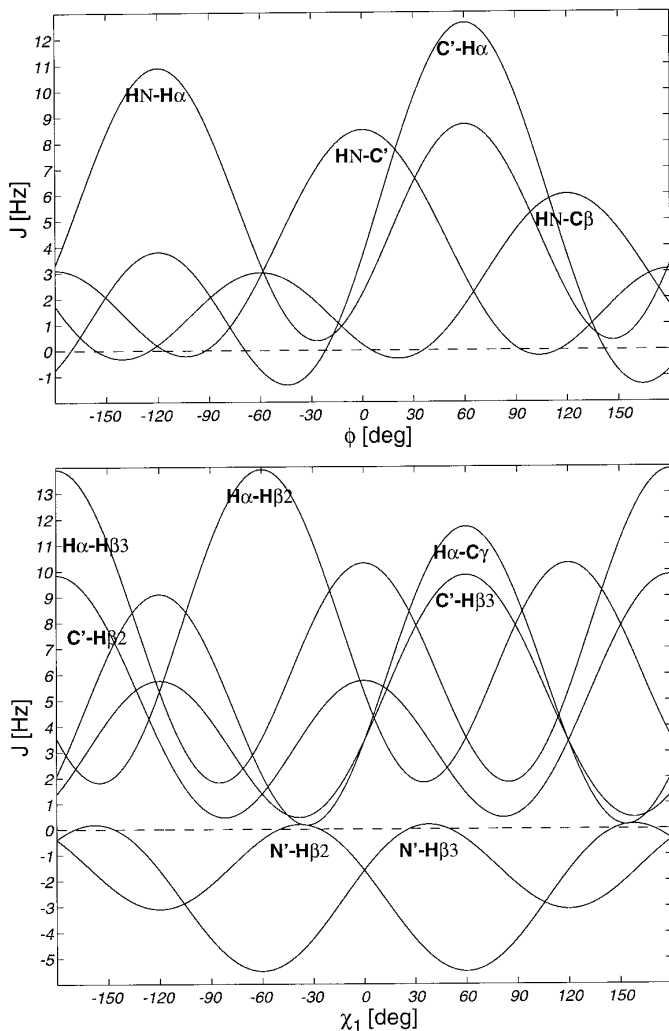
FIG. 1. Dependence of various homo- and heteronuclear ^3J coupling constants on the backbone dihedral angle ϕ (top) and on the side-chain dihedral angle χ_1 (bottom). Karplus coefficients in the equation $^3J = A \cos^2\theta + B \cos\theta + C$ were used as given in Table 1. Note that some pairs of the Karplus curves show a correlated angle dependence, thus reducing the amount of independent structure information.

dundant information. Particular topological arrangements which possess an internal symmetry, e.g., the ϕ dihedral-angle environment in the glycine residue, preclude finding a unique solution for any specified set of coupling constants. The analysis must then refer to independent data like NOE distance information in order to resolve the mirror-image problem.

Previous coupling analysis has been based on the assumption that a single rigid molecular conformation prevails. Due to local conformational mobility and intramolecular reorientation processes (19), both NOE cross-relaxation rates and J coupling constants represent dynamically averaged parameters (20). If more than the minimum number of coupling constants are available, the excess information can be used to detect and characterize angular conformational equilibria.

In the presence of rapid angular interconversion, the experimental coupling constant is averaged over distinct dihedral-angle states θ weighted by individual probabilities $p(\theta)$ as given by

$$\langle J \rangle = \int_0^{2\pi} p(\theta)J(\theta)d\theta. \qquad [2]$$

In these circumstances, the derivation of angular constraints is no longer unambiguous, and due interpretation of experimental data requires conformational flexibility be taken into account. As shown in Fig. 2, the presence of internal molecular mobility leads to discrepancies between the experimental (averaged) ^3J coupling constant and that expected from a fixed dihedral angle which can easily exceed the experimental uncertainty obtained in numerical J evaluation. The present study aims at the investigation of dihedral-angle distributions based on accurately determined J values. The work refers to the companion paper (21) in which high-precision ^3J coupling constants in the naturally occurring peptide antamanide were gathered from various references, in particular $^3J_{HC}$ coupling constants from heteronuclear relayed E.COSY (22).
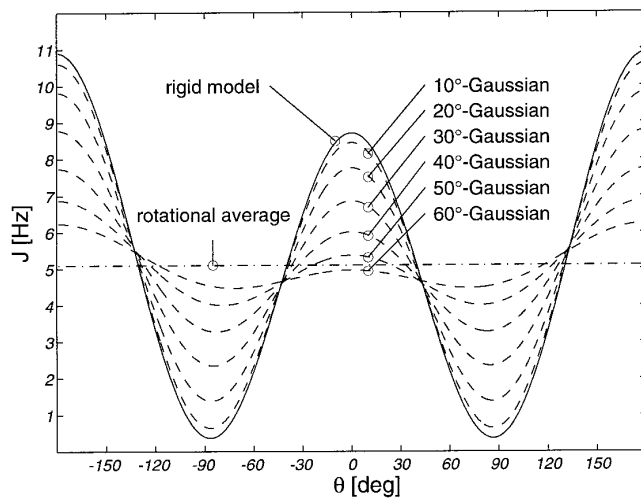
FIG. 2. The influence of local mobility on the observed average ^3J coupling constants. Shown is the dependence of the $^3J(H^N, H^\alpha)$ coupling constant on the dihedral angle $\theta(H^N, H^\alpha) = \phi - 60°$ for various extents of torsion-angle fluctuation according to a unimodal Gaussian mode. The solid line (—) shows the original Karplus curve for the parameter set $A = 9.4$ Hz; $B = -1.1$ Hz; $C = 0.4$ Hz inserted into Eq. [1] and is valid in the limit of a strictly rigid torsion. Weighting (convolution) of this Karplus curve by a Gaussian normal distribution for the torsion angle, $p(\theta)$ in Eq. [2], with varying spread in the dihedral angle, σ_θ in Eq. [5], yields expectation values for the conformationally averaged coupling constants displayed by dashed lines (- - -). The limit of uniform occupancy of all dihedral-angle states, i.e., rotational averaging, leads to the mean ^3J coupling constant (-·-), which was calculated to be 5.1 Hz from the given coefficients according to $\langle J \rangle_\theta = A/2 + C$. It is evident that in the reverse process of dihedral-angle determination from J-coupling information, the neglect of conformational averaging may lead to significant misinterpretation of the J coupling constant with respect to dihedral-angle geometry.

The cyclic peptide antamanide (−Val[1]−Pro[2]−Pro[3]−Ala[4]−Phe[5]−Phe[6]−Pro[7]−Pro[8]−Phe[9]−Phe[10]−), isolated from the toxic mushroom *Amanita phalloides* (*23*), has been investigated by a variety of analytical methods (*24–27*) and is among the best characterized peptide compounds with respect to both conformational equilibria and dynamic properties. Kessler and co-workers were the first to propose a collective two-site conformational interconversion in the antamanide backbone, based on the combined interpretation of homonuclear NOE and $^3J(H^N, H^\alpha)$ coupling constants (*28*). Interconversion times in microseconds for the backbone mode (*29–32*), in nanoseconds for the motion in the phenylalanine side chains (*33, 34*), and in picoseconds for the proline rings (*35–37*) were found. Such detailed structural knowledge renders antamanide an excellent reference compound for studies of the feasibility and limits of quantitative structure determination based on high-precision three-bond coupling constants.

METHODS

The J Residual

A unique torsion-angle rotamer can be viewed as the limiting case of completely frozen internal mobility, but generally angular orientation is not necessarily restricted to a single rotameric state. Hence, conformational analysis in the presence of internal molecular motion requires more than one dihedral-angle value to be adjusted in order to minimize the following figure of merit, termed the *J* residual,

$$\epsilon_J^2 = \sum_k \sigma_k^{-2} \{J_k^{\text{expt}} - \langle J_k^{\text{calc}} \rangle\}^2$$
$$= \sum_k \sigma_k^{-2} \{J_k^{\text{expt}} - \sum_l [p(\theta_l) J_k^{\text{calc}}(\theta_l)]\}^2, \qquad [3]$$

where *k* signifies a coupled spin pair and *l* runs over the conformations considered. J^{expt} and J^{calc} are the experimental coupling constant and that calculated from a model, respectively. The contribution from the particular coupling constant J_k to the error is properly weighted by its specific experimental uncertainty σ_k.

Any solution to the probability-distribution function $p(\theta_l)$ that reduces ϵ_J^2 below a given threshold, e.g., the sum of variances in the coupling constants measured, is accepted to fulfill a set of experimental *J* values. The number of potential models for internal mobility appears unlimited because the dihedral-angle resolution might be chosen arbitrarily, and the fractional occurrence of each of the contributing conformations may have any value between 0 and 1 while satisfying the constraint $\Sigma p_l = 1$. Reasonable models might be uni- or multimodal Gaussian profiles, or ensembles of discrete dihedral-angle conformations, or mixtures thereof. In practice, the complexity of the model is restricted so as to leave a nonvanishing number of available degrees of freedom as determined by the difference between the number

of coupling constants measured and the number of adjustable model parameters. In the following, various simple models of internal motion (denoted R, G, B, and S) are applied to the case of antamanide in order to discover the most probable distribution of dihedral-angle rotameric states.

Models for Dihedral-Angle Probability-Distribution Functions

The most simplistic model, a rigid conformation (R) has a single fixed dihedral angle θ with probability $p(\theta) = 1$, and $p = 0$ otherwise. In this framework, θ is the only adjustable parameter to minimize the difference between calculated and experimental coupling constants according to the hypothesis

$$J_k^{\text{expt}} \equiv J_k^{\text{calc}}(\theta + \Delta\theta_k), \qquad [4]$$

where *k* indicates the pair of the coupled nuclei according to Table 1.

In an improved model (G), additional local dihedral-angle fluctuation about the mean dihedral angle might be considered. From relaxation measurements and molecular dynamics studies (*19*), it is evident that even in a well-defined conformation the dihedral angle librates by approximately ±10°. The internal molecular motion then leads to an averaging of the involved ^3J values as indicated by Eq. [2]. This effect might be modeled by a Gaussian-shaped distribution function for $p(\theta)$ and is shown in Fig. 2. The dihedral-angle search including local mobility according to a unimodal Gaussian distribution (*38, 39*) thus requires a two-parameter fit of mean $\overline{\theta}$ and deviation σ_θ, as given by

$$J_k^{\text{expt}} \equiv J_k^{\text{calc}}(\overline{\theta}, \sigma_\theta)$$
$$= \frac{1}{\sigma_\theta \sqrt{2\pi}} \int_{-\pi}^{+\pi} J_k(\theta + \Delta\theta_k)$$
$$\times \exp\left\{\frac{(\theta + \Delta\theta_k - \overline{\theta})^2}{2\sigma_\theta^2}\right\} d\theta. \qquad [5]$$

Alternatively, the conformational characterization can be extended to a two-state equilibrium associated with a bistable jump process (B). Accordingly, two dihedral angles as well as a population ratio are varied in a three-parameter fit of θ_1, θ_2, and p_1 used as

$$J_k^{\text{expt}} \equiv J_k^{\text{calc}}(\theta_1, \theta_2, p_1)$$
$$= p_1 J_k(\theta_1 + \Delta\theta_k) + (1 - p_1) J_k(\theta_2 + \Delta\theta_k). \qquad [6]$$

Often, the side-chain χ_1 rotamer analysis is restricted to the energetically favored staggered conformations according to Pachler (*40, 41*), where χ_1 adopts distinct values of −60°, ±180°, and +60°, designated by either I, II, and III or alternatively t^2g^3, g^2t^3, and g^2g^3, respectively. The latter nomenclature signifies also diastereospecific proton positions. These
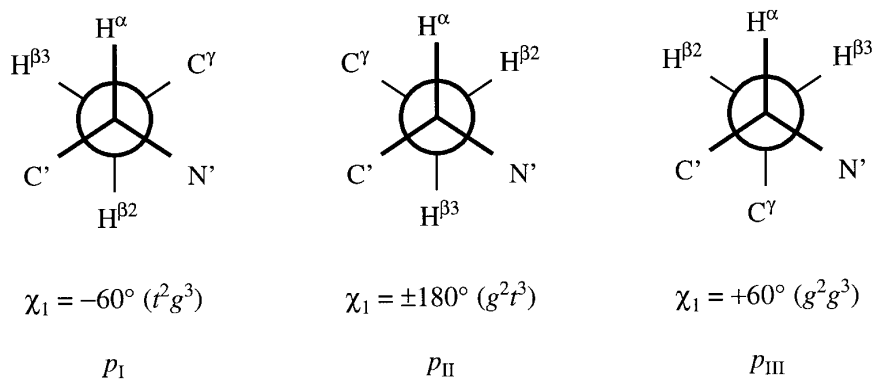
FIG. 3. Newman projections of the staggered side-chain conformers. Shown is the situation in the majority of the amino-acid residues bearing two protons in the C^β position. The C^γ atom is substituted for $H^{\beta 1}$, O^γ, and S^γ in alanine, serine, and cysteine residues, respectively. In valine, the patches are $C^\gamma \to C^{\gamma 1}$, $H^{\beta 2} \to C^{\gamma 2}$, $H^{\beta 3} \to H^\beta$, in contrast to isoleucine where it is $C^\gamma \to C^{\gamma 2}$, $H^{\beta 2} \to C^{\gamma 1}$, $H^{\beta 3} \to H^\beta$, while in threonine $C^\gamma \to C^{\gamma 2}$, $H^{\beta 2} \to O^{\gamma 1}$, $H^{\beta 3} \to H^\beta$. In any case, the torsion-angle value is taken from the orientation of the highest-rank substituent, γ or $\gamma 1$, with respect to the main-chain atom N' following Ref. (13).

particular conformations are shown in Fig. 3. In a three-site jump between staggered states (S), the χ_1 values are fixed while the set of populations p_I, p_{II}, and p_{II} is allowed to vary, leading to a two-parameter fit of p_I and p_{II}, according to

$$
\begin{aligned}
J_k^{\text{expt}} &\equiv J_k^{\text{calc}}(p_I, p_{II}) \\
&= p_I J_k(-60° + \Delta\theta_k) + p_{II} J_k(\pm 180° + \Delta\theta_k) \\
&\quad + (1 - p_I - p_{II}) J_k(+60° + \Delta\theta_k),
\end{aligned}
\tag{7}
$$

where the condition constraining p_{III} is included.

A pictorial representation of typical probability-distribution functions associated with the models is given in Fig. 4. If sufficient experimental coupling constants are available, more complicated models, e.g., multimodal or skewed Gaussian distributions, can be applied. However, the number of geometry variables would exceed the number of available J values in the antamanide test case.

COMPUTATIONS

To identify the backbone and side-chain conformations in antamanide, the experimental (averaged) ^3J coupling constants (21, 26, 32, 42) served as targets in least-squares optimizations of the parameters θ, or $\bar{\theta}$ and σ_θ, or θ_1, θ_2, and p_1, or p_I and p_{II}, according to the models R, G, B, and S, respectively. The experimental ^3J coupling constants at hand [Table 2 from Ref. (21)], together with the Karplus parameters and phase increments given in Table 1, were inserted into Eqs. [4] through [7] for minimizing the residual given in Eq. [3]. The Simplex algorithm (43) was used for parameter optimization. To speed up numerical iteration of the Gaussian integral in Eq. [5], the approximation proposed by Brüschweiler and Case (44) was employed. Finally, probability-distribution profiles were obtained for each conforma-

tionally relevant ϕ and χ_1 dihedral angle. Results are given in Table 2 and Table 3 for side-chain and main-chain conformations, respectively.

Qualitatively, the significance of each regression manifests in a small residual ϵ_J^2, or more conveniently, in the derived quantity RMSD$_J$, the RMS difference between simulated and experimental coupling constants. Nevertheless, we prefer normalized significance measures in order to select in favor of the simpler model in case two profiles yield identical residuals while differing solely in the number of adjustables. Based on the *absolute* violation of experimental constraints, a test of the incomplete Gamma probability-distribution function within the framework of χ^2 statistics (45) affords such a quality criterion $Q_{\text{abs}} = 1 - \Gamma(\epsilon_J^2/2, \nu/2)$. This criterion accounts for the varying numbers of degrees of freedom $\nu = n - p$ in the different motional models, where n and p are the numbers of coupling constants and model parameters, respectively. Practice showed that the individual deviations between calculated and experimental coupling constants are often larger than the respective uncertainties in the reference values, possibly due to systematic errors in the set of coupling constants, in the Karplus parameters, or from substituent effects. For these reasons, Q_{abs} is considered to be too stringent for the fit significance because it rapidly approaches zero. A more modest quality criterion, which avoids normalizing the individual J-coupling violations to unit variance, is obtained by using the incomplete Beta probability-distribution function (45, 46) as given by

$$
Q_{\text{rel}} = 1 - B[F, (p - 1)/2, \nu/2],
\tag{8}
$$

where the Fisher variance ratio

$$
F_{[p-1,n-p]} = \frac{\sum_k \{J_k^{\text{calc}} - J^{\text{mean}}\}^2}{\sum_k \{J_k^{\text{calc}} - J_k^{\text{expt}}\}^2}
\tag{9}
$$
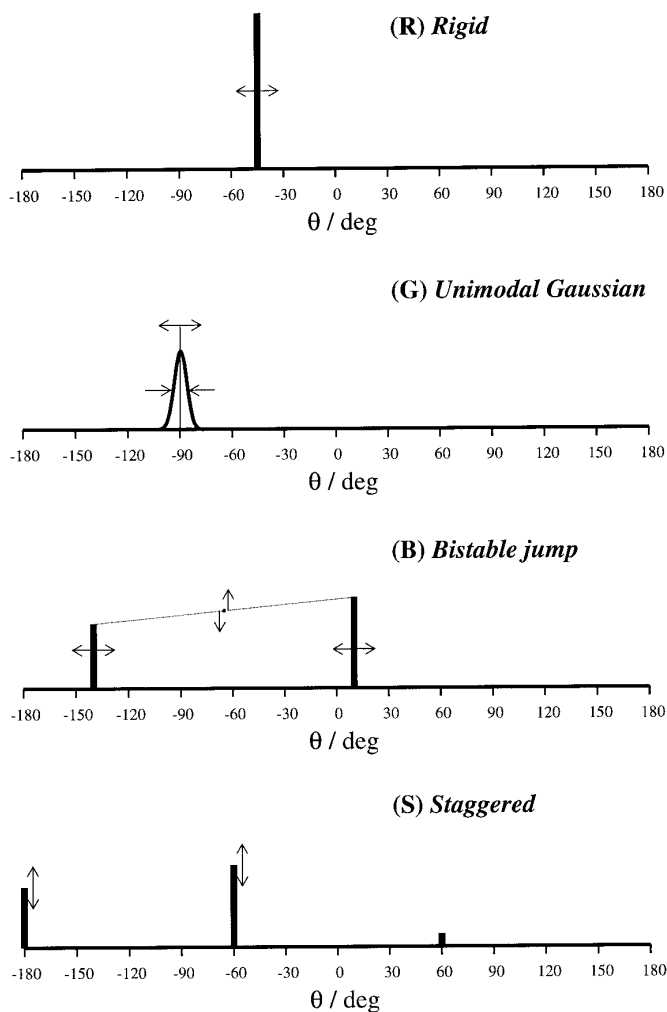
FIG. 4. Schematic representation of probability-density functions due to different motional models as used in the analysis of dihedral-angle equilibria based on ^3J coupling constants. Typical probability density functions are displayed for a rigid conformation (R), a Gaussian distribution (G), a two-site jump (B), and a Pachler-type staggered-rotamer model (S) as described in the text.

relates the sum of squares due to model-parameter effects to the sum of squares of residuals. J_k^{expt} and J_k^{calc} have their usual meanings, and J^{mean} is the average J-coupling value needed to balance the whole data set. For the rigid-rotamer search with a single variable, the number of degrees of freedom in Eq. [9] must be set to 1. Finally, the quality factors $Q = Q_{\text{rel}}$, which supplement the results given in Table 2 and Table 3, determine the confidence level that the respective model is not a result of chance arrangement in the data set.

RESULTS

Side-Chain Conformations in Antamanide

The side chains of residues Phe[5], Phe[6], Phe[9], Phe[10], and Val[1] in antamanide give rise to rotational degrees of freedom

about the dihedral angle χ_1. Rotameric states of the phenylalanine side-chain dihedral angle χ_1 were characterized by the coupling constants $J(\text{H}^\alpha, \text{H}^{\beta 2})$, $J(\text{H}^\alpha, \text{H}^{\beta 3})$, $J(\text{C}', \text{H}^{\beta 2})$, $J(\text{C}', \text{H}^{\beta 3})$, and $J(\text{H}^\alpha, \text{C}^\gamma)$. The correct analysis of the rotamer populations requires stereospecific assignments (SSA) of the phenylalanine $\text{H}^{\beta 2}$ and $\text{H}^{\beta 3}$ resonances. Partial assignments have been obtained previously for Phe[9] and Phe[10] (47). An unambiguous solution to this problem would entail the stereospecific deuteration of selected H^β sites. Because such samples were not available, the side-chain rotamer analysis was carried out twice, once for each of the two possible assignments SSA$_1$ and SSA$_2$, where SSA$_1$ maps the *low*-field $\text{H}^{\beta x}$ and the *high*-field $\text{H}^{\beta y}$ resonance to the diastereotopic positions $\text{H}^{\beta 2}$ and $\text{H}^{\beta 3}$, respectively, while assignment SSA$_2$ permutes the mapping.

For each phenylalanine residue, the five quantitative J values permitted simultaneous stereospecific H^β resonance assignment and optimization of the χ_1 dihedral-angle geometry. Figure 5 shows the error profiles obtained in a rigid-rotamer search for the two possible stereospecific assignments. As summarized in Table 2, $-17.0°$, $-119.5°$, $-54.3°$, and $-43.2°$ emerged for χ_1 in Phe[5], Phe[6], Phe[9], and Phe[10], with residual deviations of the experimental coupling constants of 1.59, 1.07, 0.55, and 1.35 Hz, respectively. SSA$_2$ was found to be the most likely stereospecific assignment for Phe[5], Phe[6], and Phe[9], while it was clearly SSA$_1$ in the case of Phe[10]. For all phenylalanines except Phe[9], a Gaussian dihedral-angle distribution or a conformation pair fitted the data significantly better than a single fixed state; i.e., allowing for local mobility in the dihedral angle reduced the discrepancy between calculated and experimental coupling constants. Table 2 also summarizes these geometry parameters calculated for the phenylalanine side chains using different motional models. In conclusion, while the side-chain χ_1 motion in Phe[10] is best characterized by a Gaussian mode, those in Phe[5] and Phe[6] are likely to be conformational equilibria between at least two distinct χ_1 conformations to account for J-averaging effects. The preliminary stereospecific assignments suggested by the rigid-model approach were also confirmed.

Interestingly, for the Phe[9] and Phe[10] side-chain conformations, a definite numerical discrimination between the various motional models is precluded because all confidence levels are larger than 90%. In fact, the geometries obtained with different models agree. According to a staggered-rotamer analysis, both Phe[9] and Phe[10] side chains prefer state I, in which $\chi_1 \approx -60°$, with minor contributions from states II ($\chi_1 = 180°$) and III ($\chi_1 = +60°$). These findings were already indicated by the large dispersion in the pair of homonuclear $^3J(\text{H}^\alpha, \text{H}^{\beta 2})$ and $^3J(\text{H}^\alpha, \text{H}^{\beta 3})$ coupling constants (42). The relative magnitudes of the $^3J(\text{H}^{\beta 2}, \text{C}')$ and $^3J(\text{H}^{\beta 3}, \text{C}')$ coupling constants found in a prior analysis made by Kessler and co-workers (47) were confirmed by the recent heteronuclear relayed E.COSY (21) study. In addition, the $^3J(\text{H}^\alpha,$
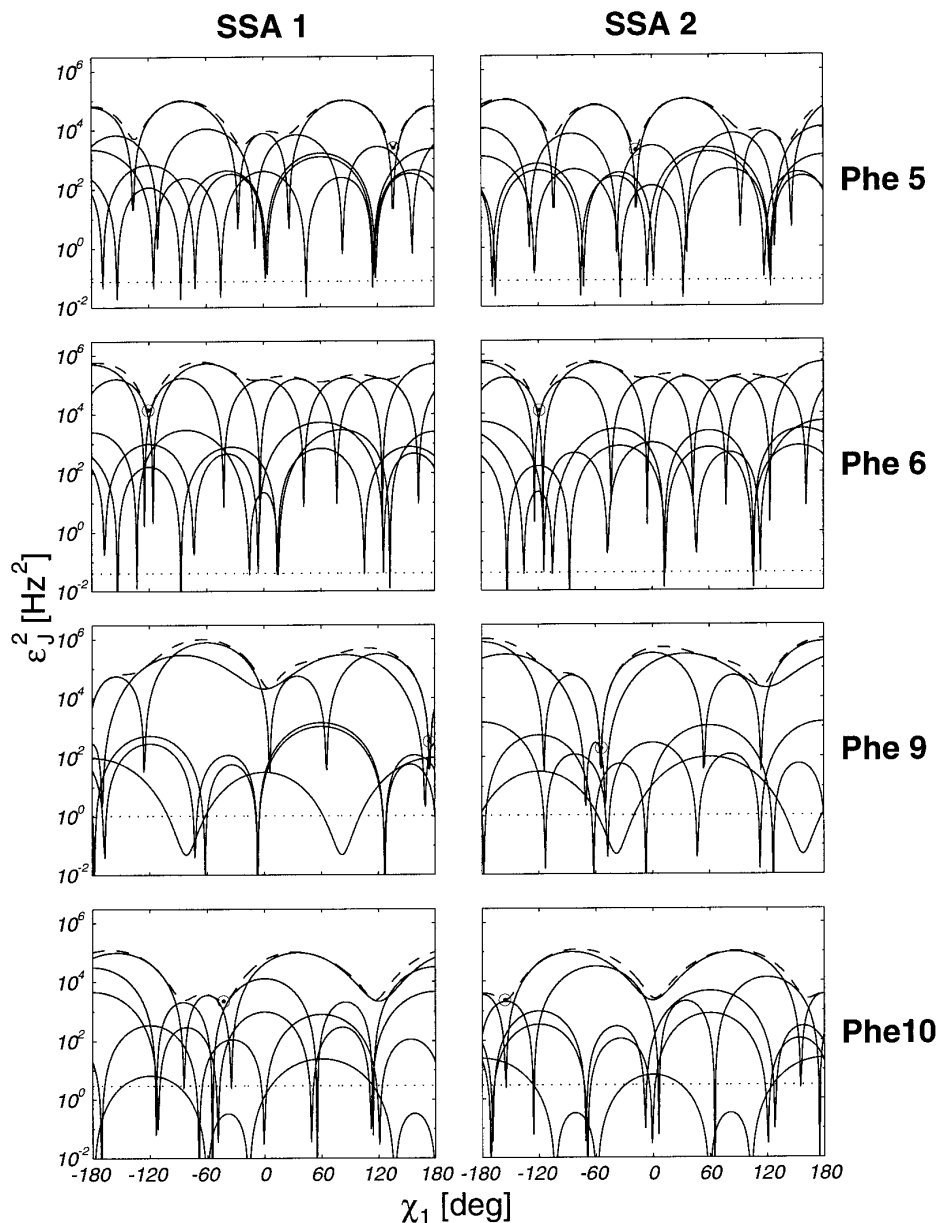
FIG. 5. Error profiles for a rigid-rotamer search of the χ_1 dihedral angle in phenylalanine residues in antamanide. Residuals between calculated and experimental coupling constants are shown for a sweep of the dihedral angle over a 2π interval according to model R described in the text. The calculation was performed for two possible stereospecific assignment SSA_1 and SSA_2 as indicated. Arcs (—) show the error profiles obtained for each individual coupling where the sinks (typically four per line) represent those dihedral angles that are in agreement with the respective coupling constant. The envelope (---) is the accumulated error according to Eq. [3], the minimum of which, the encircled dot, is the global dihedral-angle solution in the framework of the applied probability-density function (model R in this figure). The horizontal lines ($\cdots$) are the summed variances of the experimental coupling constants and thus represent the target for a 100% confidence level based on the J residual ϵ_J^2.

C^γ) coupling constants obtained agree with the proposed conformations.

For Phe[5] and Phe[6], the analysis of the side-chain rotamers is not as straightforward since both $J(H^\alpha, H^\beta)$ couplings in Phe[5] and Phe[6] exhibit intermediate magnitudes more likely due to pronounced averaging effects. Conformational equilibria between at least two staggered χ_1 dihedral-angle states are inferred. If applied to Phe[6], the Gaussian model yields

a width of $\pm 56°$ which basically amounts to the limit of full rotational averaging (Fig. 2). Indeed, the staggered-rotamer model indicates conformations I, II, and III in a 1:1:2 ratio for the dihedral angle χ_1 in Phe[6]. The Phe[5] side chain fits any of the models G, B, or S equally well. Rotational diffusion within a $\pm 40°$ Gaussian width about a distorted mean dihedral angle close to the eclipsed conformation $\chi_1 = 0°$ cannot be safely distinguished from a three-site jump be-

TABLE 2

Rotamer Distribution of Phenylalanine Side-Chain χ_1 Dihedral Angles in Antamanide According to Various Models Based on Experimental $^3J_{HH}$ and $^3J_{HC}$ Coupling Constants[a]

Rigid model

Residue	SSA$_1$ RMSD$_J$ (Hz)	Q (%)	Conformation χ_1 (°)	SSA$_2$ RMSD$_J$ (Hz)	Q (%)	Conformation χ_1 (°)	X-ray[b] χ_1 (°)
Phe^5	2.23	55.6	+136.7	1.59	77.5	−17.0	−51.1
Phe^6	1.92	16.9	−120.5	1.07	32.9	−119.5	−65.3
Phe^9	4.33	36.1	+174.4	**0.55**	**99.7**	**−54.3**	−69.0
Phe^{10}	1.35	93.1	−43.2	3.76	44.2	+163.1	−47.5

Unimodal Gaussian model[c]

Residue	SSA$_1$ RMSD$_J$ (Hz)	Q (%)	Conformation $\overline{\chi_1}$ (°)	$\sigma(\chi_1)$ (°)	SSA$_2$ RMSD$_J$ (Hz)	Q (%)	Conformation $\overline{\chi_1}$ (°)	$\sigma(\chi_1)$ (°)
Phe^5	1.35	49.1	+142.2	42.5	0.19	99.6	−22.0	40.1
Phe^6	1.72	18.5	+44.5	56.7	0.49	74.0	+73.5	56.1
Phe^9	4.21	31.3	+175.3	9.8	0.56	99.1	−55.2	9.5
Phe^{10}	**0.40**	**99.3**	**−63.1**	**26.2**	3.11	36.0	−176.2	26.1

Bistable jump model[d]

Residue	SSA$_1$ RMSD$_J$ (Hz)	Q (%)	Conformation θ_1 (°)	p_1 (%)	θ_2 (°)	p_2 (%)	SSA$_2$ RMSD$_J$ (Hz)	Q (%)	Conformation θ_1 (°)	p_1 (%)	θ_2	p_2 (%)
Phe^5	0.80	68.7	−21.9	67.2	+35.6	32.8	**0.01**	**100.0**	**−23.9**	**60.5**	**−114.7**	**39.5**
Phe^6	1.11	37.0	−109.5	73.5	−171.8	26.5	**0.33**	**83.2**	**+25.2**	**61.0**	**−78.9**	**39.0**
Phe^9	3.23	26.4	+0.4	146.0	−110.3	−46.0	0.53	96.9	−57.5	92.5	+141.3	7.5
Phe^{10}	0.39	97.3	−75.5	69.9	+140.6	30.1	2.89	21.4	−164.7	64.8	−15.1	35.2

Staggered-rotamer model[e]

Residue	SSA$_1$ RMSD$_J$ (Hz)	Q (%)	Rotamer populations p_I (%)	p_{II} (%)	p_{III} (%)	SSA$_2$ RMSD$_J$ (Hz)	Q (%)	Rotamer populations p_I (%)	p_{II} (%)	p_{III} (%)
Phe^5	1.25	55.3	33.2	47.6	19.2	0.15	99.8	48.2	34.0	17.8
Phe^6	1.54	20.2	24.5	26.3	49.2	0.46	74.1	25.8	24.2	50.0
Phe^9	4.20	31.5	7.4	96.2	−3.6	0.48	99.4	96.4	7.4	−3.8
Phe^{10}	0.45	99.0	81.1	7.3	11.6	3.05	36.8	6.8	81.1	12.1

[a] Experimental coupling constant $J(H^\alpha, H^{\beta 2})$, $J(H^\alpha, H^{\beta 3})$, $J(H^{\beta 2}, C')$, $J(H^{\beta 3}, C')$, and $J(H^\alpha, C^\gamma)$ as well as standard deviations from Ref. (*21*) and the corresponding Karplus parameters from Table 1 were used. Assignment SSA$_1$ maps *low-field* and *high-field* Hβ resonances to H$^{\beta 2}$ and H$^{\beta 3}$, respectively, and SSA$_2$ is the reversed assignment (naming conventions follow the IUPAC-IUB recommendations). RMSD$_J$ is the residual RMS violation between fitted and experimental J coupling constants, boldface indicates the best agreement based on the quality criterion Q defined in the text.

[b] Calculated from fractional heavy-atom Cartesian coordinates given in Ref. (*24*).

[c] $\overline{\chi_1}$ and $\sigma(\chi_1)$ denote Gaussian mean dihedral angle and distribution width, respectively.

[d] θ_i and p_i signify distinct dihedral-angle conformations and their populations, respectively.

[e] Conformations I, II, and III refer to staggered side-chain rotamers with $\chi_1 = -60°$, $\pm 180°$, $+60°$.

tween staggered states. However, a two-site jump with a 6:4 population ratio was found to yield the smallest errors for both side chains.

The dihedral angle χ_1 in the Val^1 side chain is determined by four coupling constants, including $J(H^\alpha, H^\beta)$, $J(C', H^\beta)$, $J(H^\alpha, C^{\gamma 1})$, and $J(H^\alpha, C^{\gamma 2})$. Two stereospecific assignments for the methyl C$^\gamma$ (and H$^\gamma$) resonances are possible. Application of all four motional models discussed led to the unequivocal stereospecific assignment SSA$_2$, according to which (C$^{\gamma 1}$, H$^{\gamma 1}$) and (C$^{\gamma 2}$, H$^{\gamma 2}$) resonance pairs are located *high*

TABLE 3
Rotamer Distribution of Main-Chain ϕ Dihedral Angles in the Nonproline Residues in Antamanide
According to Various Motional Models Based on Experimental $^3J_{HH}$ and $^3J_{HC}$ Coupling Constants[a]

Residue	Rigid model			Unimodal Gaussian model[b]				Bi-stable jump model[c]						X-ray[d]
	RMSD$_J$ (Hz)	Q (%)	ϕ (°)	RMSD$_J$ (Hz)	Q (%)	$\bar{\phi}$ (°)	$\sigma(\phi)$ (°)	RMSD$_j$ (Hz)	Q (%)	ϕ_1 (°)	p_1 (%)	ϕ_2 (°)	p_2 (%)	ϕ (°)
Val[1]	0.69	94.1	−84.1	**0.12**	**99.6**	**−98.1**	35.5	0.22	88.6	−90.3	57.1	−163.2	42.9	−109.2
	0.68	94.4	−84.5	**0.12**	**99.6**	**−99.0**	35.9	0.13	92.7	−112.5	62.6	−52.4	37.4	
Phe[6]	0.78	90.1	−160.4	**0.26**	**97.4**	**−153.6**	35.6	0.44	73.5	−155.3	54.9	−74.3	45.1	−79.6
	0.76	92.1	−158.1	**0.20**	**98.5**	**−111.7**	50.4	0.19	87.7	−102.8	67.6	−29.4	32.4	
Ala[4]	**0.15**	**100.0**	**−91.5**	0.15	99.6	−92.0	6.2	0.20	91.3	−95.5	93.2	+154.5	6.8	−108.3
	0.15	**100.0**	**−91.4**	0.14	99.6	−91.8	6.1	0.14	98.6	−92.1	97.5	−175.8	2.5	
Phe[9]	**0.09**	**100.0**	**−89.4**	0.05	99.9	−88.9	−8.1[e]	0.23	97.2	−95.3	89.9	−135.1	10.1	−106.9
	0.09	**100.0**	**−89.3**	0.05	99.9	−88.8	−8.1[e]	0.03	98.6	−89.0	101.6	−14.3	−1.6[e]	
Phe[5]	2.24	38.5	−81.8	1.95	37.6	−92.6	34.7	1.98	5.6	−116.3	54.7	−56.9	45.3	+72.6
	2.18	42.3	−83.0	1.92	39.9	−96.2	36.6	**0.51**	**69.6**	**−81.6**	**68.3**	**+49.6**	**31.7**	
Phe[10]	2.78	32.7	−158.0	2.70	25.6	−155.9	18.8	**0.22**	**88.6**	**−160.0**	**54.3**	**+59.3**	**45.7**	+57.9
	2.35	58.1	−144.6	1.49	49.7	+53.6	43.6	**0.07**	**96.4**	**−160.1**	**50.8**	**+58.9**	**49.2**	

[a] Experimental coupling constants $J(H^N, H^\alpha)$, $J(H^N, C^\beta)$, $J(H^N, C')$, and $J(C'_{i-1}, H^\alpha)$ as well as standard deviations from Ref. (21) and the corresponding Karplus parameters from Table 1 were used. RMSD$_J$ is the residual RMS violation between fitted and experimental J coupling constants, boldface indicate best agreement based on the quality criterion Q defined in the text. Statistical weights σ_J of the $J(C'_{i-1}, H^\alpha)$ coupling constant were 1.0 and 0.2 Hz for top and bottom rows, respectively.
[b] $\bar{\phi}$ and $\sigma(\phi)$ denote Gaussian mean dihedral angle and distribution width, respectively.
[c] θ_i and p_i signify distinct dihedral-angle conformations and their populations, respectively.
[d] Calculated from heavy-atom Cartesian coordinates given in Ref. (24).
[e] Negative Gaussian distribution width and population conform with rigid conformation (see text).

field and *low* field, respectively, i.e., at (ω_C, ω_H) coordinates in ppm of (17.9, 1.00) and (19.4, 1.05). While the rigid-rotamer search hints at a sterically unfavorable eclipsed conformation in which $\chi_1 \approx 120°$, the staggered-rotamer model yielded the best fit with 54% significance and RMSD$_J$ = 0.95 Hz. According to this model, the Val[1] side chain flips between the staggered rotamers depicted in Fig. 3 with populations of 47%:34%:19%. The predominant rotamer agrees with the conformation found in the solid state ($\chi_1 = -54$, 5°) (24), while angular flexibility was anticipated from the results of relaxation studies. With respect to the peculiarities of the valine side-chain conformational analysis, the reader is also referred to a detailed study of valine-related ^3J coupling constants in a protein (39).

Backbone Conformations in Antamanide

The heteronuclear ^3J coupling constants associated with the ϕ dihedral angles [Table 2 of Ref. (21)] confirm the pseudo-C_2 symmetry of the antamanide backbone proposed by some investigators (28, 30, 32). Inspection of the homonuclear $J(H^N, H^\alpha)$ coupling constants reveals a narrow range of intermediate values between 6.5 and 8.6 Hz. It had been previously concluded that these coupling constants cannot be in agreement with a unique energetically favored conformation of the cyclic peptide backbone and that they more likely represent dynamically averaged data (28–32). The

extended set comprising both homo- and heteronuclear coupling constants allows a detailed interpretation of the conformational heterogeneity for each residue.

A clear preference for negative ϕ-angle values was found in all nonproline torsions ϕ_1, ϕ_4, ϕ_5, ϕ_6, ϕ_9, and ϕ_{10} (Fig. 6). Except for ϕ_4 and ϕ_9, large J residuals were found in a rigid-rotamer search for the optimum ϕ dihedral angles (Table 3). The torsion angle ϕ_9 fits the experimental constraints with remarkably small error, which was reduced even if a Gaussian model with an artificially narrowed motional well (44) was applied. In contrast, extensive Gaussian random motion with angular averaging over a width of ±35° was indicated for ϕ_1 and ϕ_6. The backbone torsions of the preceding residues, ϕ_5 and ϕ_{10}, could not be fitted acceptably by simple models, neither by a rigid-rotamer nor by a Gaussian-motion model. They are likely to undergo a collective two-site conformational interconversion giving rise to at least two backbone equilibrium conformations. While ϕ_{10} was easily adjusted to two distinct conformations, −160° and +59° in an approximate 1:1 ratio, ϕ_5 gave unacceptable fits with either of the applied models.

Detailed comparison of the main-chain target coupling constants in Phe[5] and Phe[10] (21) revealed differences outside the experimental limits and indicates breaking of the pseudo-C_2 symmetry. However, deviation from experimental data in Phe[5] was found to depend critically on the weighting of the $^3J(H^\alpha, C'_{i-1})$ coupling constant. Originally, this particular
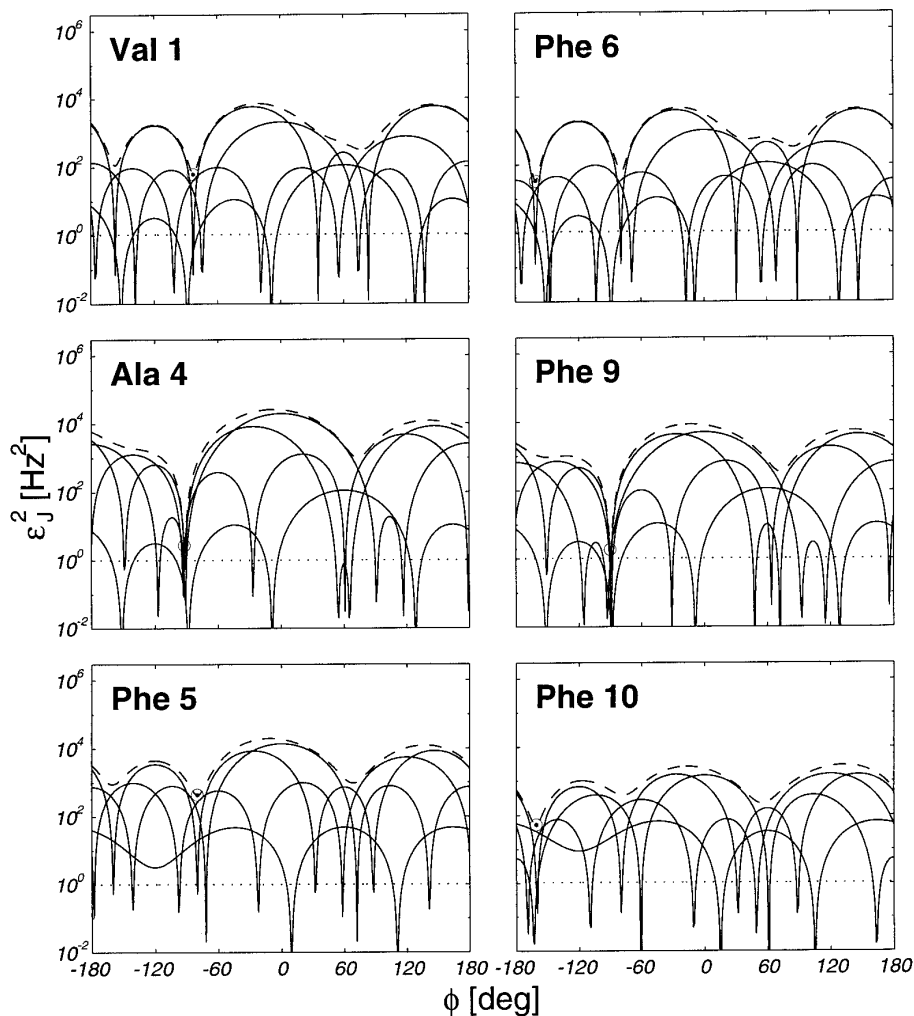
FIG. 6. Error profiles obtained in rigid-rotamer searches for the torsions ϕ in antamanide. Smallest errors are found for negative dihedral angle values. Note the pairwise similar profiles exhibiting the pseudo-C_2 symmetry of the compound. For further details see the legend to Fig. 5.

coupling was only roughly determined with an uncertainty of 1 Hz (*32*). Such a large standard deviation essentially removes the respective coupling constant from the set of experimental constraints. When weighting was arbitrarily increased by a factor of 5, i.e., a precision of 0.2 Hz was assumed, acceptable ϕ_5 backbone geometries were obtained with the bistable-jump model. Accordingly, the backbone ϕ torsion of Phe[5] adopts negative and positive values of $-82°$ and $+50°$ in an approximate 2:1 ratio, although a superposition of three conformations cannot be excluded (Fig. 7). Alternative weighting of the $^3J(H^\alpha, C'_{i-1})$ coupling constant was also applied to the previous optimizations in order to check the influence on the results (Table 3). Although the trends were maintained for the other residues, significant reduction in the residuals was observed, especially for the three-parameter model *B*. Interestingly, the rigid conformation detected for Phe[9] was emphasized upon heavier weighting of the $^3J(H^\alpha, C'_{i-1})$ coupling constant even in the two-site jump model.

DISCUSSION

According to the quantitative coupling analysis, flexibility in the antamanide backbone is found at four out of six possible ϕ torsions. Experimental J data are fulfilled when both torsions ϕ_5 and ϕ_{10} adopt equilibria between distinct rotamers, and when both torsions ϕ_1 and ϕ_6 exhibit a broad contin-
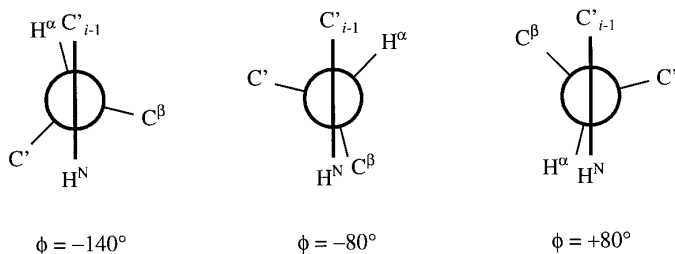
FIG. 7. Newman projections of typical states of the backbone torsions ϕ encountered in the nonproline residues in antamanide.

uous dihedral-angle distribution, while torsions ϕ_4 and ϕ_9 are nearly rigid. Based on a previous combined study of homonuclear NOE and $^3J(H^N, H^\alpha)$ coupling constants, Kessler and co-workers (28) suggested a conformational equilibrium of so-called $(+, +)$ and $(-, -)$ backbone conformations indicating that the particular dihedral angles ϕ_5 and ϕ_{10} simultaneously interconvert between two states with values of approximately $+80°$ and $-80°$ (Fig. 7). Multiconformational evaluation of distance information using a stochastically constrained minimization algorithm, i.e., the MEDUSA protocol (32), revealed many alternative 1:1 admixtures of backbone pair structures of antamanide that are also capable of fulfilling the experimental NOE and coupling constraints at various specified significance levels.

Note that in the present coupling study, NOE cross-relaxation information was intentionally disregarded. The comparatively small number of 24 backbone-associated high-precision J values was sufficient to reproduce ensemble properties emerging from the 936-sample MEDUSA analysis (32), which was based on 23 quantitative NOE distance constraints as well as 82 qualitative lower distance bounds. Similarly, as few as 24 high-precision J values associated with side-chain torsions made it possible to access detailed ensemble properties of the phenylalanine and valine side chains.

Similar side-chain conformations of Phe[9] and Phe[10] have been previously deduced, but conclusions about the Phe[5] and Phe[6] side chains were drawn in a tentative manner (47). Quantifications were based exclusively on pairs of homonuclear $^3J(H^\alpha, H^\beta)$ coupling constants. These two experimental quantities allowed at most a two-parameter model to be applied, for example, the Pachler-type analysis. The absence or presence of cross peaks in COLOC spectra, taken as a support for the conclusions reached, is certainly unsuited for incorporation into a numerical evaluation procedure. The present approach is more extensive as five quantitative coupling constants, together with error estimates, are included to aim at quantitative χ_1 populations for any of the phenylalanine side chains in antamanide. More elaborate protocols that utilize force-field evaluations in conjunction with time-averaged coupling restraints (48) are currently applied to obtain dihedral-angle distribution profiles for comparison with the present results.

A few comments on the staggered-rotamer model are in order, because this model is traditionally applied in qualitative analysis of side-chain torsion angles. In the staggered-rotamer analysis (model S), the torsion angles are constrained to specific values, a fact which imposes severe limitations on the conformational characterization of a dihedral-angle distribution. Although the assumption of staggered rotamers is reasonable from energetic considerations, high-resolution X-ray studies (49, 50) indicate that amino-acid side chains in proteins do occur in twisted conformations and are not necessarily constrained to staggered states. The Pachler-type analysis may therefore be an oversimplifi-

cation when characterizing amino-acid side-chain geometries in polypeptides. As demonstrated in the conformational analysis of the Phe[5] and Phe[6] side chains, the staggered-rotamer model was ruled out by a variable-angle model with an even larger number of adjustables. On the other hand, modeling side-chain equilibria by three-state jumps between staggered conformations is equivalent to the use of continuous probability-distribution models, as exemplified with all phenylalanines in antamanide.

As long as a comprehensive theory of the J-coupling phenomenon is lacking, rotamer analysis depends not only on the accuracy and precision of the coupling constants but also on the set of Karplus coefficients selected in the spectrum-structure transformation protocol. To conform with prior investigations (28, 32, 47), particular sets of Karplus coefficients were used as specified in Table 1. Although alternative sets of Karplus coefficients are available, a quantitative estimate of the influence of different parametrizations on dihedral-angle constraints is beyond the scope of this work. It has been demonstrated elsewhere (39) that the determination of conformational equilibria depends on the parameters actually used. Often, Karplus coefficients are calculated from dihedral angles obtained from high-resolution X-ray analysis, although it is very likely but not at all certain that both solution and crystal structure are identical. The present work might serve as an example: In chloroform solution, the major antamanide backbone conformation with negative values for ϕ_5 and ϕ_{10} agrees better with the X-ray structure of the antamanide–alkaline–ion complex (25) rather than with the crystal structure of the H_2O complex (24), which matches the minor conformation with positive values for ϕ_5 and ϕ_{10}.

Although rigid torsions gave satisfactory fits to the experimental coupling constants in a few instances, for 8 out of 11 torsional angles in antamanide, unimodal Gaussian χ_1-angle distributions (model G) or two-site jump models (model B) fit the experimental coupling constants significantly better than the simple rigid-angle model. The improvement of the fit is a consequence of allowing for dihedral-angle fluctuations connected with an averaging of the calculated J coupling constants toward intermediate values. In fact, for moderate variations ($\sigma_\theta = 5–10°$), e.g., ϕ in Ala[4] and χ_1 in Phe[9], the effect of averaging on the calculated coupling constants is smaller than the precision of the experimental coupling constants, while larger scatter of θ ($\sigma_\theta > 15°$) has significant impact (Fig. 2).

With respect to dynamic effects, one might argue that empirical determinations of Karplus coefficients refer to model compounds that also exhibit—to a limited extent—angular oscillation and that the coefficients themselves are therefore expected to account for averaging effects (51). An impressive example is the optimization of the backbone ϕ geometry in Phe[9] (Table 2). Numerical modifications have been devised to remove small-amplitude random-motion effects from the empirical Karplus curves (44), based on the

critical assumption that force-field calculations properly reflect molecular-dynamics phenomena. In order to avoid cyclic rationalization, such corrections were not applied in the present analysis, although it was known that angular excursions of more than $\pm 10°$ might lead to significant distortion of the ^3J coupling constant. Severe effects are expected if the mean dihedral angle is associated with extreme, either large or small, ^3J coupling constants (Fig. 2).

In the course of relaxation studies (*52, 53*), it has been suggested to separate the width of the local vibrational well from the peaked distribution due to distinct potential-energy minima. Accordingly, model R lacks both effects, and model G ignores the multiple conformational minima, while models B and S ignore the problem of finite width within each minimum. Indeed, such simplifications were demonstrated by the difficulties in adjusting the geometry of the backbone torsion ϕ_5. Combinations of these two phenomena are conceivable, although it appears questionable whether a clear-cut distinction exists. Molecular dynamics studies on proline residues in antamanide (*37*) showed that in the unambiguous presence of both phenomena, two-site jump reorientation and high-frequency libration, small jump-reorientation angles are occasionally concealed by the average local-fluctuation amplitude, which means that the two vibrational wells are hardly separated.

However, an improved approximation of the dihedral-angle probability-distribution function by skewed or multimodal Gaussian models (*38*) with more than two adjustable model parameters requires use of an extended set of observables. Tests with a simple trimodal Gaussian model (S–G) comprising two populations for the staggered conformations and a single global width were found to converge extremely poorly. As a consequence of the inherent symmetry in the set of the constituent *trans* and *gauche* coupling constants, the model parameters were fully correlated and usually yielded 1:1:1 ratios and an incredibly large narrowing factor of $\sigma_\theta \approx -100°$. Similar observations were made when a four-parameter model (B–G) of a bistable jump combined with a uniform Gaussian libration mode was applied to the phenylalanine χ_1 torsions. Obviously, the five coupling constants available represent less than five effective constraints, and application of these complicated motional models gave rise to ambiguous solutions as a consequence of the rapidly exhausted degrees of freedom. Exploiting other structural data, such as experimental NOE cross-relaxation rates, in addition to coupling constants has been shown to lead to continuous probability distributions of rotamers in amino acids using the recently developed method CUPID (*54, 55*). Alternatively, empirical force-field potentials including time-dependent torsion-angle restraints compiled from ^3J coupling constants (*48*) have been utilized in molecular-dynamics simulations to provide more information.

In liquid-state NMR spectroscopy, the three-dimensional model of a polypeptide chain is usually generated under the assumption of an isotropically reorienting rigid molecular arrangement. This restriction allows straightforward translation of spectral parameters into conformational parameters, and vice versa, the back-calculation of spectral responses from geometry information. Abandoning the rigid-molecule simplification, the amount of experimental data required for a detailed characterization of a flexible molecular structure rapidly increases with molecular size (*56*). Fitting dihedral angles to a set of experimental ^3J coupling constants suffers mainly from the attempt to characterize a possibly very complex ensemble of conformations on the basis of only a few coupling constants. Nevertheless, it was demonstrated that thorough ^3J-coupling analysis allows detailed insight into time-independent local conformational equilibrium properties and thus complements relaxation measurements which explore the time dependence of conformational interconversion (*31, 33*).

CONCLUSIONS

In the presence of conformational flexibility, the derivation of dihedral-angle constraints from coupling information requires that ^3J values be determined at the highest attainable accuracy and precision. Transformation procedures have been devised to derive accurate molecular geometries from experimental ^3J coupling information, with particular emphasis on the inclusion of molecular internal mobility. While intentionally disregarding NOE structural information, the rigorous *J*-coupling analysis was shown to reproduce the conformational flexibility of the sample peptide antamanide which had been found from quantitative analysis of relaxation data. Two backbone conformations in a dynamic exchange equilibrium are sufficient to agree with the set of averaged coupling constants associated with the backbone ϕ torsions. The conformations of two out of four phenylalanine side chains are found to involve at least two distinct side-chain rotameric states. The solution side-chain conformations found for phenylalanines 5 and 6 and valine 1 show a larger spread than those found in the solid state. The case of antamanide demonstrates that particular polypeptide conformations may be trapped during crystallization, thereby representing only part of the conformational space accessible in solution.

REFERENCES

1. K. Wüthrich, ''NMR of Proteins and Nucleic Acids,'' Wiley, New York, 1986.

2. R. R. Ernst, G. Bodenhausen, and A. Wokaun, ''Principles of Nuclear Magnetic Resonance in One and Two Dimensions,'' Clarendon Press, Oxford, 1987.

3. N. J. Oppenheimer, and T. L. James (Eds.), ''Nuclear Magnetic Resonance. Part A: Spectral Techniques and Dynamics; Part B: Structure and Mechanism,'' Methods in Enzymology, Vols. **176/ 177**, Academic Press, San Diego, 1989.

4. A. Bax, *Annu. Rev. Biochem.* **58**, 223 (1989).

5. G. Wagner, *Prog. NMR Spectrosc.* **22**, 101 (1990).

6. G. C. K. Roberts (Ed.), ''NMR of Macromolecules: A Practical Approach,'' Oxford Univ. Press, Oxford, 1993.

7. D. A. Case, H. J. Dyson, and P. Wright, *Methods Enzymol.* **239,** 392 (1994).

8. C. Biamonti, C. B. Rios, B. A. Lyons, and G. T. Montelione, *Adv. Biophys. Chem.* **4,** 51 (1994).

9. M. Eberstadt, G. Gemmecker, D. M. Mierke, and H. Kessler, *Angew. Chem.* **107,** 1813 (1995); *Angew. Chem. Int. Ed.* **34,** 1671 (1995).

10. D. Neuhaus and M. Williamson, ''The Nuclear Overhauser Effect in Structural and Conformational Analysis,'' VCH, New York, 1989.

11. T. L. James, *Curr. Opin. Struct. Biol.* **1,** 1042 (1991).

12. T. L. James, *Curr. Opin. Struct. Biol.* **4,** 275 (1994).

13. IUPAC-IUB Commision on Biochemical Nomenclature, *J. Mol. Biol.* **52,** 1 (1970); *Biochemistry* **9,** 3471 (1970).

14. M. Karplus, *J. Chem. Phys.* **30,** 11 (1959).

15. M. Karplus, *J. Am. Chem. Soc.* **85,** 2870 (1963).

16. V. F. Bystrov, *Prog. NMR Spectrosc.* **10,** 41 (1976).

17. P. E. Hansen, J. Feeney, and G. C. K. Roberts, *J. Magn. Reson.* **17,** 249 (1975).

18. V. F. Bystrov, Yu. D. Gavrilov, and V. N. Solkan, *J. Magn. Reson.* **19,** 123 (1975).

19. C. Brooks, M. Karplus, and B. M. Pettitt, *in* ''Proteins: A Theoretical Perspective of Dynamics, Structure, and Thermodynamics,'' *Adv. Chem. Phys.* Vol. **71,** Wiley, New York, 1988.

20. O. Jardetzky, *Biochem. Biophys. Acta* **621,** 227 (1980).

21. J. M. Schmidt, *J. Magn. Reson.* **124,** 298 (1997).

22. J. M. Schmidt, R. R. Ernst, S. Aimoto, and M. Kainosho, *J. Biomol. NMR* **6,** 95 (1995).

23. T. Wieland and H. Faulstich, *Crit. Rev. Biochem.* **5,** 185 (1978).

24. I. L. Karle, T. Wieland, D. Schermer, and H. C. J. Ottenheym, *Proc. Natl. Acad. Sci. USA* **76,** 1532 (1979).

25. I. L. Karle, *J. Am. Chem. Soc.* **96,** 4000 (1974).

26. H. Kessler, A. Müller, and K.-H. Pook, *Liebigs Ann. Chem.* 903 (1989).

27. H. Kessler, J. W. Bats, J. Lautz, and A. Müller, *Liebigs Ann. Chem.* 913 (1989).

28. H. Kessler, C. Griesinger, J. Lautz, A. Müller, W. F. van Gunsteren, and H. J. C. Berendsen, *J. Am. Chem. Soc.* **110,** 3393 (1988).

29. R. R. Ernst, M. Blackledge, S. Boentges, J. Briand, R. Brüschweiler, M. Ernst, C. Griesinger, Z. L. Mádi, T. Schulte-Herbrüggen, and O. W. Sørensen, in ''Proteins: Structure, Dynamics and Design,'' (V. Renugopalakrishnan, P. R. Carey, I. C. P. Smith, S. G. Huang and A. C. Storer, Eds.), p. 11, ESCOM, Leiden, 1991.

30. R. Brüschweiler, M. Blackledge, and R. R. Ernst, *J. Biomol. NMR* **1,** 3 (1991).

31. R. Brüschweiler, B. Roux, M. Blackledge, C. Griesinger, M. Karplus, and R. R. Ernst, *J. Am. Chem. Soc.* **114,** 2289 (1992).

32. M. J. Blackledge, R. Brüschweiler, C. Griesinger, J. M. Schmidt, Ping Xu, and R. R. Ernst, *Biochemistry* **32,** 10960 (1993).

33. T. Bremi, M. Ernst, and R. R. Ernst, *J. Phys. Chem.* **98,** 9322 (1994).

34. T. C. Beutler, T. Bremi, R. R. Ernst, and W. F. van Gunsteren *J. Phys. Chem.* **100,** 2637 (1996).

35. Z. L. Mádi, C. Griesinger, and R. R. Ernst, *J. Am. Chem. Soc.* **112,** 2908 (1990).

36. R. M. Brunne, W. F. van Gunsteren, R. Brüschweiler, and R. R. Ernst, *J. Am. Chem. Soc.* **115,** 4764 (1993).

37. J. M. Schmidt, R. Brüschweiler, R. R. Ernst, R. L. Dunbrack, Jr., D. Joseph, and M. Karplus, *J. Am. Chem. Soc.* **115,** 8747 (1993).

38. J. C. Hoch, C. M. Dobson, and M. Karplus, *Biochemistry* **24,** 3831 (1985).

39. Y. Karimi-Nejad, J. M. Schmidt, H. Rüterjans, H. Schwalbe, and C. Griesinger, *Biochemistry* **33,** 5481 (1994).

40. K. G. R. Pachler, *Spectrochim. Acta* **19,** 2085 (1963).

41. K. G. R. Pachler, *Spectrochim. Acta* **20,** 581 (1964).

42. C. Griesinger, O. W. Sørensen, and R. R. Ernst, *J. Magn. Reson.* **75,** 474 (1987).

43. J. A. Nelder, and R. Mead, *Computer J.* **7,** 308 (1965).

44. R. Brüschweiler and D. A. Case, *J. Am. Chem. Soc.* **116,** 11199 (1994).

45. W. H. Press, B. P. Flannery, S. A. Teukolsky, and W. T. Vetterling, ''Numerical Recipes,'' Cambridge Univ. Press, Cambridge, 1989.

46. M. Abramowitz, and I. A. Stegun, ''Handbook of Mathematical Functions,'' *Applied Mathematics Series,* Vol. **55,** National Bureau of Standards, Washington, DC; reprinted Dover, New York, 1968.

47. H. Kessler, C. Griesinger, and K. Wagner, *J. Am. Chem. Soc.* **109,** 6927 (1987).

48. A. E. Torda, R. M. Brunne, T. Huber, H. Kessler, and W. F. van Gunsteren, *J. Biomol. NMR* **3,** 55 (1993).

49. J. Janin, S. Wodak, M. Levitt, and B. Maigret, *J. Mol. Biol.* **125,** 357 (1978).

50. J. W. Ponder and F. M. Richards, *J. Mol. Biol.* **193,** 775 (1987).

51. L. J. Smith, C. Redfield, and C. M. Dobson, *Biochemistry* **30,** 986 (1978).

52. G. Lipari and A. Szabo, *J. Am. Chem. Soc.* **104,** 4546 (1982); *J. Am. Chem. Soc.* **104,** 4559 (1982).

53. G. M. Clore, A. Szabo, A. Bax, L. E. Kay, P. C. Driscoll, and A. M. Gronenborn, *J. Am. Chem. Soc.* **112,** 4989 (1990).

54. Z. Dzakula, W. M. Westler, A. Edison, and J. Markley, *J. Am. Chem. Soc.* **114,** 6195 (1992).

55. Z. Dzakula, A. Edison, W. M. Westler, and J. Markley, *J. Am. Chem. Soc.* **114,** 6200 (1992).

56. R. R. Ernst, *Angew. Chem.* **104,** 817 (1992); *Angew. Chem. Int. Ed.* **31,** 805 (1992).